Journal of Nuclear Materials 424 (2012) 261–276

Contents lists available at SciVerse ScienceDirect

Journal of Nuclear Materials

journal homepage: www.elsevier.com/locate/jnucmat

Oxidation behavior of ferritic–martensitic and ODS steels in supercritical water

Jeremy Bischoff*, Arthur T. Motta

Department of Mechanical and Nuclear Engineering, Pennsylvania State University, 227 Reber Building, University Park, PA 16802, USA

ARTICLE INFO

Article history:
Received 23 December 2011
Accepted 6 March 2012
Available online 14 March 2012

ABSTRACT

Ferritic–martensitic and ODS alloys are primary candidates for application as cladding and structural materials in the Generation IV Supercritical Water Reactor. One of the main in-service degradation mechanisms for these alloys is uniform corrosion. This article analyzes the oxide microstructure formed on these alloys to better understand their oxidation behavior. Corrosion tests were performed in both steam and supercritical water (SCW) at 500 and 600 °C. The oxide microstructure was analyzed using microbeam synchrotron radiation diffraction and fluorescence associated with electron microscopy. The oxide forms a three-layer structure with an outer layer containing only Fe_3O_4, an inner layer containing a non-uniform $(Fe,Cr)_3O_4$ spinel structure, and a diffusion layer containing a mixture of metal grains and chromium-rich precipitates. A marker experiment located the original water–metal interface as the outer–inner layer interface implying a mechanism where iron migrates outwards to form the outer layer and oxygen diffuses inwards to form the inner layer.

1. Introduction

1.1. Motivation

The Supercritical Water Reactor is one of the six Generation IV nuclear power plant designs and was envisioned for its high thermal efficiency and simplified core [1]. This reactor is designed to function at high outlet temperature (between 500 °C and 600 °C), which requires cladding and structural materials that can perform at these elevated temperatures for extended exposures. Because of their resistance to void swelling under irradiation and to stress corrosion cracking, ferritic–martensitic steels, such as HCM12A and NF616, are candidate materials for this application [2]. Oxide dispersion strengthened (ODS) alloys such as the 9CrODS (JAEA) and the 14CrODS (CEA) steels are ferritic–martensitic steels that contain a fine dispersion of yttrium–titanium-rich oxide nanoparticles inside their matrix. The ODS alloys were developed initially for applications in the sodium-cooled fast reactor [3–5]. Although ODS steels exhibit enhanced corrosion resistance compared to conventional ferritic–martensitic alloys [6,7] ferritic–martensitic alloys corrode faster overall than other alloys. Therefore their uniform corrosion has to be better understood in order to mitigate it. This is the focus of this article.

The present article reviews previous results on the oxide layer structure to give an overview of the oxidation behavior of these alloys in supercritical water (SCW) and analyzes these results to give some insight on the corrosion mechanism [8–12]. The oxide layers formed during exposure to SCW were characterized using microbeam synchrotron radiation diffraction and fluorescence, scanning electron microscopy (SEM), and transmission electron microscopy (TEM) using energy filtered imaging (EFTEM) and electron energy loss spectroscopy (EELS). Considering all these results we analyze the formation process of these oxide layers and discuss the corrosion mechanism.

1.2. Review of various oxidation mechanisms

Between the 1960s and the early 1980s various oxidation mechanisms were proposed to explain the formation of dual oxide layers observed for Fe–Cr and Ni–Cr alloys in various environments including sulfur, carbon dioxide, water (liquid and gas) and O_2. A recent review of the models was performed by Martinelli [13–17]. The models can be classified into three distinct types: the formation of the inner layer by dissociation of the outer layer, the formation of a dual layer due to differences in diffusion rates, and finally the "available space" model.

The first corrosion models concerning the formation of dual layers originated from Wagner and were based on the dissociation of the outer oxide to form the inner layer [18,19]. In both models proposed by Wagner, the oxide forms by outward migration of cations. The inward diffusion of oxygen does not come into play because the models correspond to an outward growth of two layers. Consequently, the original water–metal interface is neither the outer–inner layer interface, nor the oxide–metal interface. In his study of Co–Cr alloys, Kofstad used a similar dissociation mechanism to explain a dual layer formation except that in his model the outer–inner layer interface corresponds to the original water–metal

* Corresponding author. Tel.: +1 33 6 72 38 19 37.
E-mail address: bischoff.jeremy@gmail.com (J. Bischoff).

0022-3115/$ - see front matter © 2012 Elsevier B.V. All rights reserved.
http://dx.doi.org/10.1016/j.jnucmat.2012.03.009

interface since the inner layer forms at the oxide–metal interface instead of at the outer–inner layer interface as in the Maak–Wagner model [20]. The oxygen necessary for this inward formation comes from the dissociation of the outer layer at the outer–inner layer interface as in the Maak–Wagner model. In this model, the outward diffusion of cobalt forms the CoO outer layer and leads to the formation of pores at the oxide–metal interface. The inner layer grows within the volume of these pores, in a similar manner to what is proposed in the "available space model" described below.

The second type of model involves the formation of a dual-layer oxide structure by the outward migration of cations with significantly different diffusion coefficients, as is the case in Fe–Cr alloys, where chromium diffusion is much slower than that of iron [21–23]. Such a model was proposed by Brückman, who suggested the formation of an inner layer consisting of a solid solution of $A_xB_yO_z$ and an outer layer of $A_{x'}O_{z'}$ [24]. The separation between the two layers only occurs because B diffuses much slower than A and therefore we obtain an outer layer containing only A. In this model the original water–metal interface does not correspond with any of the interfaces observed in the oxide structure after oxidation, making this model improbable since the outer–inner layer interface was shown to be the original water metal interface [12]. A similar model was proposed by Whittle and Wood for the corrosion of Fe–18Cr steels in O_2 [25]. Although their model seems inappropriate for the above reason, it brings forth an interesting aspect in the formation of the $FeFe_{2-x}Cr_xO_4$ spinel inner layer, where fluctuations of the chromium content within this layer induce variations of the outward diffusion of iron. We will further discuss this aspect in this article.

Finally, in contrast to the other models, the "available space model" considers the simultaneous diffusion of both the oxidant and the cations [26–35]. The original water–metal interface corresponds to the outer–inner layer interface in the oxide. The oxide grows both at the outer layer surface and at the oxide–metal interface. The rate-limiting step is the outward diffusion of iron, which leaves behind vacancies and pores at the oxide–metal interface, where this "available space" will be used to form new oxide. Much debate persists as to the diffusion of the oxidant through the oxide layer whether diffusion occurs as molecules or ions, through nano/micro-channels or pores. This model seems to fit well with the oxidation of ferritic–martensitic steels but it accounts neither for the formation of a diffusion layer, nor for the formation of the pores in the inner layer rather than in the metal, and moreover it assumes that the inner layer is homogeneous, which as we will see is not necessarily the case.

1.3. Description of the spinel structure

The spinel structure contains cations with two different oxidation states (2+ and 3+) bonded with oxygen ions. The normal spinel structure can be described as an FCC lattice of oxygen ions with the 2+ cation in one of the eight different tetrahedral sites and the two 3+ ions in octahedral sites, one in the central octahedral site and four other 3+ on four of the edges of the cell that are shared by 4 cells (thus resulting in a multiplicity of two 3+ ions per cell) [21,22,32,36–43]. Since there are 12 edges in the FCC cell, each shared between 4 cells (total of three sites per cell), plus the octahedral site in the center results in a total octahedral site multiplicity of 4 per FCC cell. The spinel unit cell is most often described as a combination of eight FCC cells (each with a multiplicity of 4), resulting in a multiplicity of 32, where the cations are located in specific tetrahedral and octahedral sites depending on the location of the simple FCC cell in the eight FCC cell combination. Consequently, the spinel cell contains 32 O^{2-} ions, 8 2+ cations in tetrahedral sites (out of the 64 possible sites) and 16 3+ cations in octahedral sites (out of the possible 32 sites). Thus 1/8 of the tetrahedral sites and 1/2 of the octahedral sites are taken. Fig. 1 shows a schematic of the spinel unit cell [44].

The magnetite Fe_3O_4 structure is an inverse spinel structure, which means that all the Fe^{2+} cations are in octahedral sites and are replaced in the tetrahedral sites by half of the Fe^{3+} cations. This enables rapid electron transfer between Fe^{2+} and Fe^{3+} cations in octahedral sites, a process called electron hopping, which spreads the charge over all the octahedral ions to form $(Fe^{3+})(Fe^{2.5+})_2O_4$ with Fe^{3+} in the tetrahedral sites and the $Fe^{2.5+}$ in the octahedral sites [42]. Since chromium is only present in the form of Cr^{3+}, this electron hopping process is impossible when chromium is located in the octahedral sites.

The structure of chromite $FeCr_2O_4$ is a normal spinel structure with Fe^{2+} in tetrahedral sites and the Cr^{3+} in the octahedral sites. Consequently, as the chromium content increases in an initial purely Fe_3O_4 phase to form $FeCr_2O_4$, the structure evolves gradually from inverse spinel to normal spinel. This structural change

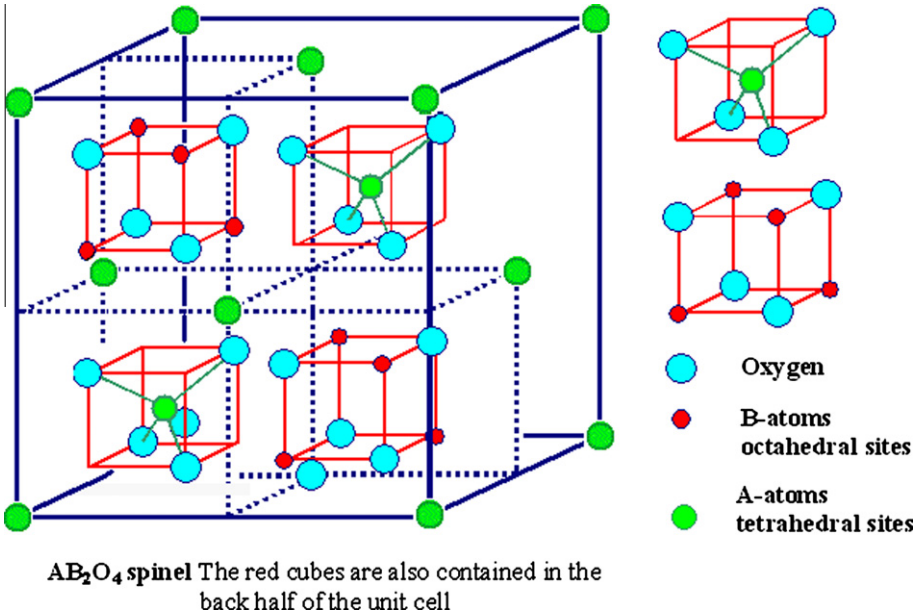

Fig. 1. Schematic of the spinel cell structure [44].

is accompanied by variations in cell parameter. The cell parameters used for the microbeam synchrotron radiation diffraction analysis match the values found in the literature for both phases (8.3775 Å for $FeCr_2O_4$ and 8.3975 Å for Fe_3O_4). Furthermore, in their study of the oxidation of magnetite into maghemite γ-Fe_2O_3 (some Fe^{3+} in tetrahedral sites compared to the corundum structure α-Fe_2O_3 where all the Fe^{3+} is in octahedral sites), Gillot et al. have shown that the structure varies depending on the chromium content x in the $(Fe^{2+}Fe^{3+}_{2-x}Cr^{3+}_{x})O^{2-}_{4}$ phase as follows [40]:

$0 < x < 0.4$: totally inverse spinel.
$0.4 < x < 1.4$: partially inverse spinel.
$1.4 < x < 2$: normal spinel.

At very low Cr content, in the inverse spinel structure, Cr replaces first the Fe^{3+} ions in the octahedral sites leading to a smaller cell parameter because of more covalent Cr–O bonds and smaller Cr ionic radius (Fe^{3+} = 64.5 pm (high-spin configuration for oxygen octahedral sites) and Cr^{3+} = 61.5 pm [89,96]). Once all the Fe^{3+} in octahedral sites has been replaced, Cr^{3+} starts to replace the Fe^{2+}in octahedral sites and forcing a Fe^{2+}/Fe^{3+} exchange in tetrahedral sites leading to an increase of cell parameter due to Fe^{2+} replacing Fe^{3+} in tetrahedral sites (the Fe^{2+} ionic radius in high spin is about 78 pm, much bigger than the Fe^{3+} radius, resulting a lattice distortion), and to a partially inverse spinel structure. Once all the Fe^{2+} has been pushed into tetrahedral sites, the structure becomes normal spinel, and additional chromium replaces the Fe^{3+} still present in octahedral sites causing a decrease in cell parameter.

The analysis of the spinel structure helps better understand the diffusion paths for the different species through the spinel structure and thus is important to understand the corrosion kinetics.

2. Experimental procedures

2.1. Alloys studied

Two commercial ferritic–martensitic alloys (NF616 and HCM12A furnished to us by the University of Wisconsin) and two ODS alloys (9CrODS and 14CrODS) were analyzed in this study. Table 1 shows the elemental composition of the alloys studied in wt% (balanced in iron). NF616 was normalized at 1070 °C for 2 h, air-cooled then tempered at 770 °C for another 2 h before final air-cooling. HCM12A was normalized at 1050 °C for 1 h, air-cooled, then tempered for 7 h at 770 °C and air-cooled. This metallurgic process creates alloys containing the martensitic lath structure and where all the carbon in solution has precipitated as $Cr_{23}C_6$ along the lath and prior austenite grain boundaries [45].

9CrODS samples were supplied by Japan Atomic Energy Agency for corrosion at the University of Wisconsin. The ODS Y_2O_3 particles were mechanically mixed with the other elements before being sealed in cans under vacuum of 0.1 Pa at 400 °C, and then hot-extruded and forged at 1150 °C. The alloy was normalized for 1 h at 1050 °C, air-cooled, and then tempered at 800 °C for 1 h. The details of the manufacturing process are described elsewhere [4]. The 14CrODS alloy was developed by the CEA in France for applications in fusion and Generation IV reactors, including the Supercritical Water Reactor (SCWR) using a similar fabrication process to that of the 9CrODS alloy [5,46]. The alloy was hot-extruded at 1100 °C, hot-rolled 20% at 650 °C and annealed at 1050 °C for 1 h [5].

The surface of the NF616, HCM12A and 14CrODS alloys was etched to reveal the alloy microstructure using a solution of 23 mL of HCl, 10 mL of HNO_3, and 18 mL of H_2O. Fig. 2 shows SEM images of the tempered martensite structure of NF616 and HCM12A and Fig. 3 shows SEM images of the 14CrODS alloy microstructure in both the normal and transverse extrusion directions. The microstructure of the 9CrODS alloy is expected to be similar to that of the 14CrODS alloy. For both NF616 and HCM12A, carbides formed at the prior austenite and martensitic lath boundaries, further outlining the grain structure. The structure of the ODS alloys is ferritic rather than tempered martensite. The ferrite grains are much smaller than the grains observed in the commercial alloys studied and appear to be slightly elongated in the extrusion direction as shown in Fig. 3. No carbides are observed along the grain boundaries.

Table 1
Elemental composition of the alloys studied in wt%. The balance is Fe.

Alloy	C	N	Al	Si	P	S	V	Cr	Ti	Mn	Ni	Cu	Nb	Mo	W	Others
NF616	.109	–	.005	.102	.009	.003	.194	8.82	–	.45	.174	–	.064	.468	1.87	O: 42 ppm
HCM12A	.11	.063	.001	.27	.016	.002	.19	10.83	–	.64	.39	1.02	.054	.3	1.89	B: 31 ppm
9CrODS	.14	–	–	.048	–	.003	–	8.6	.21	.05	.06	–	–	–	2	Y_2O_3
14CrODS	.04	–	–	.3	–	–	–	13.7	.3	.3	.2	–	–	–	2	Y_2O_3

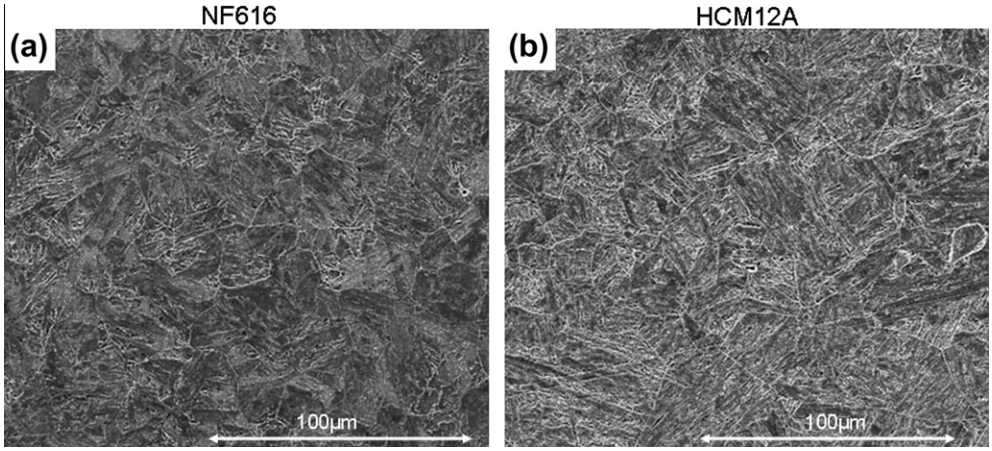

Fig. 2. SEM images of the tempered martensite structure of NF616 and HCM12A.

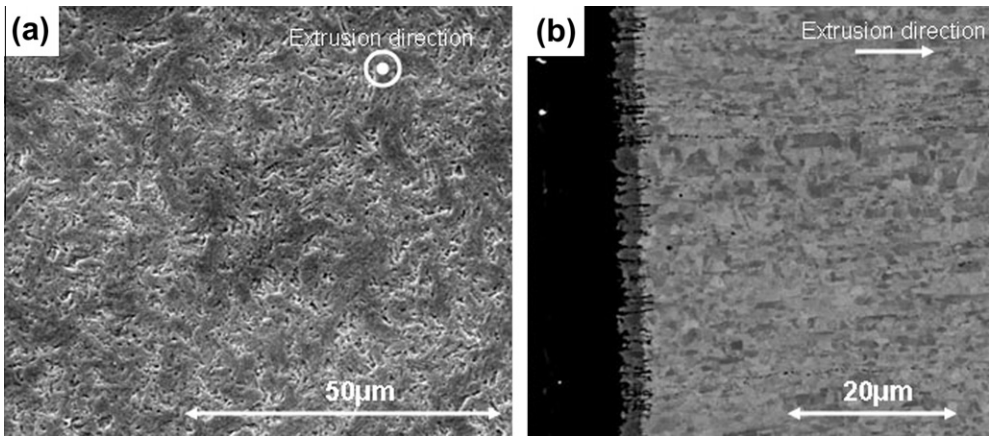

Fig. 3. SEM images of the 14CrODS alloy microstructure in both the normal and transverse extrusion directions.

2.2. Corrosion tests, marker experiment, and characterization techniques

Corrosion tests were performed in both steam and supercritical water. The steam corrosion tests were performed at Westinghouse Electric Co. in a static deaerated autoclave at a pressure of 10.8 MPa. The supercritical water tests were performed at the University of Wisconsin in a supercritical water loop at a pressure of 25 MPa. Two supercritical water tests were performed with small dissolved oxygen content in both (10–20 ppb): the first at 600 °C in a vertical loop described previously [47,48] and the second at 500 °C in a horizontal loop. It is assumed that the oxygen content in both steam and SCW is very similar. In all experiments, different coupons were used for each data point to produce the mass gain curves, where the mass gain was normalized to the surface area of the coupon (weight gain per unit area).

Prior to oxidation, the samples were all polished to 0.05 μm colloidal silica and palladium markers were also deposited on some of the samples to locate the original water–metal interface after oxidation. The photolithographic marker deposition process used for this experiment enables the deposition of an array of micrometric markers on the sample surface, as described in a previous article [12].

The main characterization technique used to analyze the oxide microstructure was microbeam synchrotron radiation diffraction and fluorescence. The synchrotron experiment and its experimental procedure have been described in previous articles [10,49–51]. In short, the synchrotron enables to scan through the oxide layer with a step size of 0.2 μm and acquire simultaneous diffraction and fluorescence data at each step. Thus it is possible to "map" the distribution of phases and elements throughout the oxide layer. Due to its high resolution, this technique can differentiate peaks associated with phases with very similar structures and lattice parameters, such as Fe_3O_4 and $FeCr_2O_4$. The distinction between these two phases is obtained through a more detailed analysis of the peaks as was done in a previous article [10].

Both scanning (SEM) and transmission (TEM) electron microscopy examination were used to complement the synchrotron experiment in the oxide characterization. The SEM images were taken using the backscatter detector of a FEI Quanta 200 ESEM. The TEM analysis of the samples was performed using a JEOL LaB_6 2010 at 200 kV. The energy filtered imaging (EFTEM) and electron energy loss spectra (EELS) were obtained on the same microscope, which is equipped with a Gatan Tridiem™ energy filter.

All the characterization techniques used 3 mm disk cross-sectional samples that were polished to 0.05 μm colloidal silica. The sample preparation technique is described in previous articles [10,50]. Additionally, the TEM samples were obtained from these 3 mm disks by using the *in situ* lift-out procedure [52] using a FEI Quanta 200 3D Dual Beam Focused Ion Beam as described previously [53,54].

3. Results

3.1. Overview of the oxide layer structure

Using microbeam synchrotron radiation diffraction and fluorescence, it is possible to obtain diffraction patterns from various locations in the oxide layers and through indexing of the diffraction peaks, infer what phases are present at these different locations. All the ferritic–martensitic and ODS steels studied exhibited a three-layer structure with an outer layer containing only Fe_3O_4, an inner layer containing a mixture of Fe_3O_4 and $FeCr_2O_4$ and a diffusion layer containing a mixture of chromium-rich oxide precipitates ($FeCr_2O_4$ and Cr_2O_3) and metal grains. Fig. 4 shows a prototypical SEM image of the oxide layers formed on ferritic–martensitic alloys, here for NF616 at 600 °C, and a schematic highlighting the main characteristics of each layer. The outer layer is formed of large columnar grains while the inner layer contains small equiaxed grains. In the diffusion layer, the oxide precipitates are located along the lath and grain boundaries, thus outlining the base metal microstructure. Whereas the outer layer has a simple structure, both the inner and diffusion layers are much more complex due to the presence of various types of oxides (Fe_3O_4, $FeCr_2O_4$, $(Fe,Cr)_3O_4$, FeO, Cr_2O_3) located in various positions in the oxide layer. Additionally, these two layers are likely to be the more protective layers since their chromium content is higher than that of the base metal and the outer layer is thought to be non-protective [10]. We will therefore focus our analysis of the oxide layer on the inner and the diffusion layers.

3.1.1. Inner layer

The inner layer contains primarily an iron-chromium spinel phase with a composition that ranges from Fe_3O_4 to $FeCr_2O_4$. Some Cr_2O_3 peaks are observed sporadically throughout the layer and more frequently at the inner-diffusion layer interface. A detailed analysis of the inner layer of the 9CrODS alloy exposed to 600 °C SCW using microbeam synchrotron radiation diffraction shows that the (3 1 1) diffraction peak from Fe_3O_4 and $FeCr_2O_4$ shifts from the $FeCr_2O_4$ location near the inner-diffusion layer interface to the Fe_3O_4 location near the outer–inner layer interface [10]. This implies a non-homogeneous distribution of phases in the inner layer

with chromium-rich phases near the inner-diffusion layer interface and iron-rich phases near the outer–inner layer interface.

This result is linked to a non-uniform distribution of elements as shown by the microbeam synchrotron fluorescence data. In most cases the inner layer exhibits an increasing chromium-to-iron ratio from the outer layer to the diffusion layer. In a few samples, a localized chromium enrichment peak is observed at the inner-diffusion layer (as was the case in the 9CrODS 600 °C 2-week sample [10]). Additionally, this gradient of chromium through the inner layer varies with exposure time, as suggested by Whittle and Wood [25]. Fig. 5 shows fluorescence plots, which illustrate the evolution of the chromium and iron content in the inner layer of HCM12A exposed to SCW for 2, 4 and 6 weeks, with corresponding SEM images. In this series of images, the 2-week sample shows a clear positive chromium gradient from the outer–inner layer interface to the inner-diffusion layer interface. In the 4-week sample the gradient is now negative and in the 6-week sample the gradient is close to 0. This shows that the inner layer structure varies with exposure time as was described in a previous article on the oxidation of the 9CrODS alloy in 600 °C SCW [10], thus making the oxidation process more complex.

Fig. 6 shows a schematic depiction of the evolution of the oxide layer microstructure of the 9CrODS steel in 600 °C SCW as a function of exposure time along with SEM images of the 2-week, the 4-week and the 6-week samples. These SEM images show the appearance of a Cr_2O_3 film at the diffusion layer-metal interface between the 2 and 4-week samples. In the inner layer, the SEM images show changes in the microstructure through the porosity

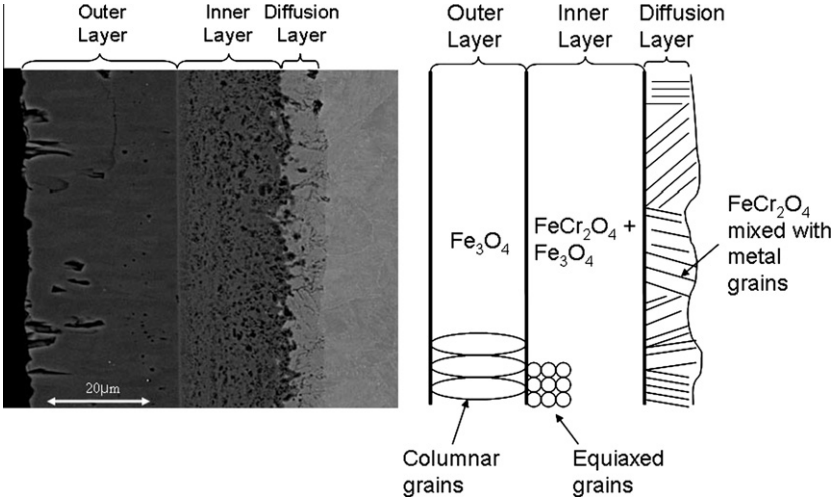

Fig. 4. SEM image of the oxide layer formed NF616 at 600 °C with a schematic highlighting the main characteristics of each layer.

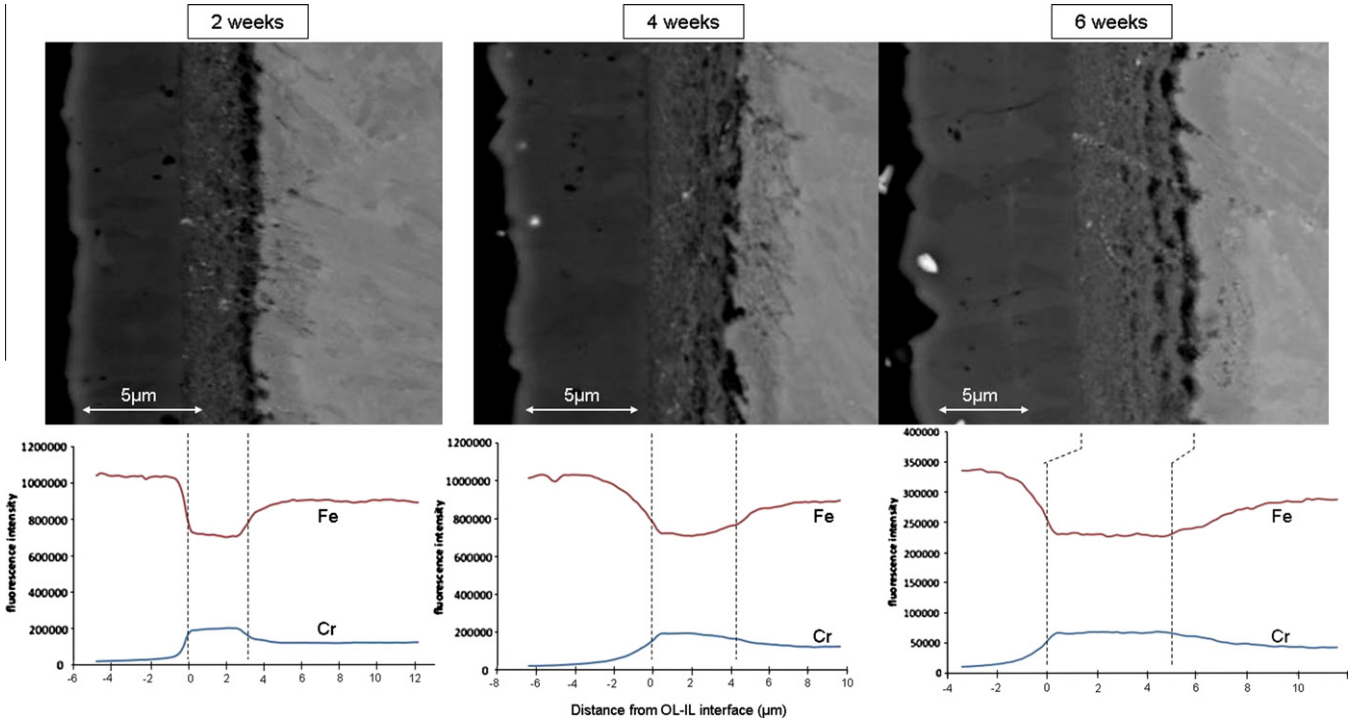

Fig. 5. Fluorescence plots showing the chromium and iron content in the inner layer of HCM12A exposed to SCW for 2, 4 and 6 weeks, with corresponding SEM images.

and straightness of the inner-diffusion layer interface. In both the 2 and 4-week samples, the porosity is mainly located right at the inner-diffusion layer interface, which is straight. In the 4-week sample, the dashed-box area has little porosity at the interface and the interface is wavier with an advancement of the inner layer into the diffusion layer. In that specific area, the interface is similar to the one observed in the 6-week sample where the porosity is more spread out through the inner layer and the inner-diffusion layer interface is wavy due to the advancement of the inner layer into the diffusion layer. These differences observed in the SEM images correspond to differences in the oxide microstructure and especially to the location of the Cr_2O_3 phase.

Figs. 7 and 8 show the contour plots of the synchrotron diffraction intensity as a function of distance in the oxide in the horizontal axis and diffraction angle 2-theta in the vertical axis for the 9CrODS 600 °C 2-week and the 6-week samples, respectively.

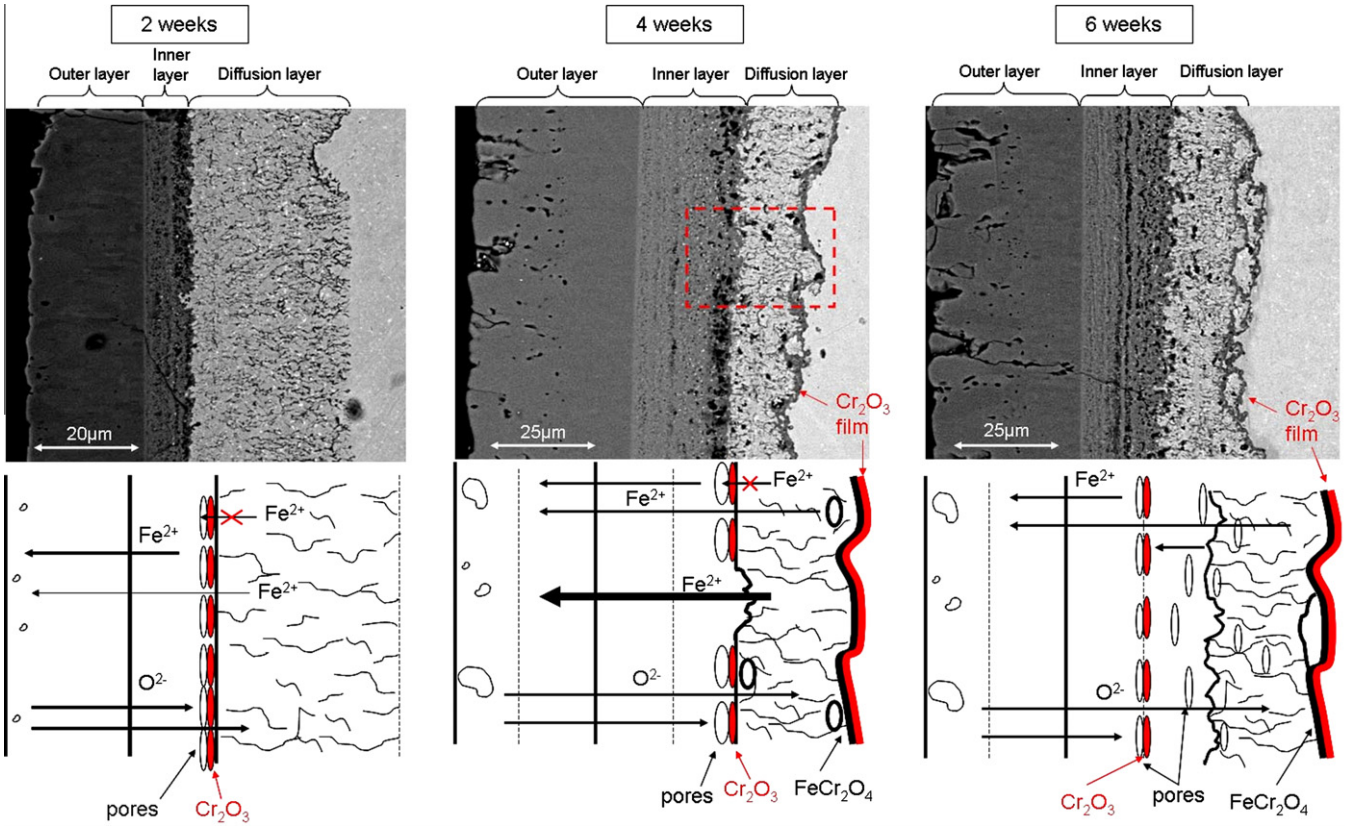

Fig. 6. SEM images and schematics of the oxide layer microstructure of the 9CrODS steel in 600 °C SCW for 2, 4 and 6-weeks.

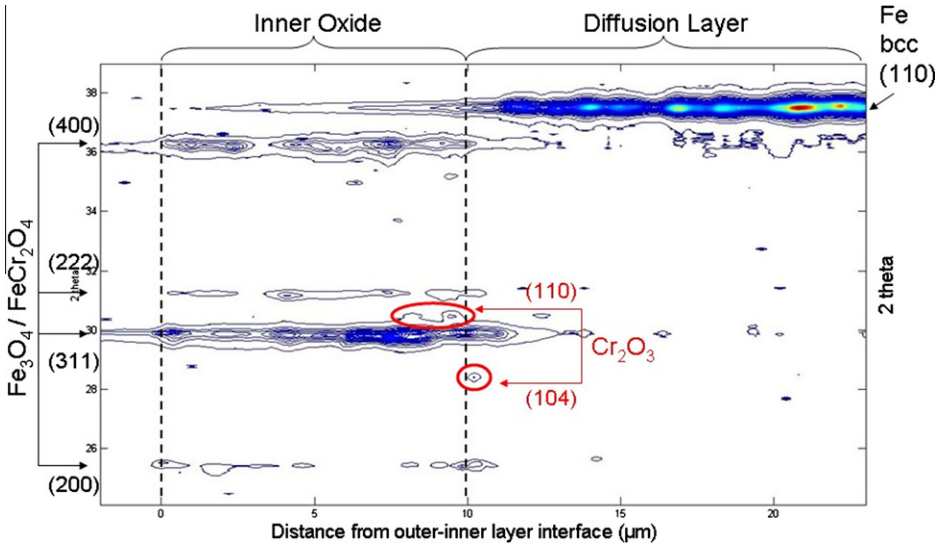

Fig. 7. Contour plot of the synchrotron diffraction intensity as a function of distance in the oxide in the horizontal axis and diffraction angle 2-theta in the vertical axis for the 9CrODS 600 °C 2-week sample.

These plots show the presence of Cr_2O_3 peaks right at the inner-diffusion layer interface for the 2-week sample but in the 6-week sample Cr_2O_3 peaks are observed further inside the inner layer, near to where a line of pores is seen in the SEM image of Fig. 6. These data suggest that the presence of Cr_2O_3 at the interface helps slow down the advancement of the inner layer into the diffusion layer, forming a straight interface and enhancing the formation of pores at the interface. This is consistent with the slower diffusion of both iron and oxygen in Cr_2O_3 compared to their diffusion in spinel [55], leading to slower advancement of the inner layer into the diffusion layer (diffusion of oxygen) and to the inability of the iron diffusing from the diffusion layer to compensate for the influx of iron vacancies leading to the formation of pores at this interface. This also suggests that areas where an increase of chromium content is observed are associated with a line of pores, which could explain the relative periodicity in porosity seen in the inner part of the inner layer.

An energy filtered TEM imaging analysis of the inner layer showed that the porosity observed in the inner layer is linked with the outward migration of iron because chromium-rich and iron-depleted zones were seen in EFTEM maps [53]. The maps in the reference article (Fig. 5 of [53]) show that chromium and iron are distributed non-uniformly within the inner layer and that the chromium-rich zones are located around pores. The close-up chromium and iron maps (Fig. 6 of [53]) show that in-between these chromium rich zones, there is an iron-chromium elemental segregation forming small nanometric chromium-rich particles. Consequently, the inner layer shows a complex structure with non-uniform distribution of elements and phases, which can influence the diffusion processes related to the oxidation mechanism.

3.1.2. Diffusion layer

The structure of the diffusion layer is also complex due to the mixture of oxide precipitates and metal grains. Fig. 9 shows two SEM images of the diffusion layer of HCM12A exposed to 600 °C SCW for (a) 2 weeks and (b) 4 weeks [11]. In both cases, the oxide formation in the diffusion layer occurs at the lath boundaries and therefore follows the base metal microstructure. These oxide precipitates are chromium-rich, mainly $FeCr_2O_4$ or Cr_2O_3 as was shown previously using synchrotron diffraction data [10] and EFTEM analysis [53].

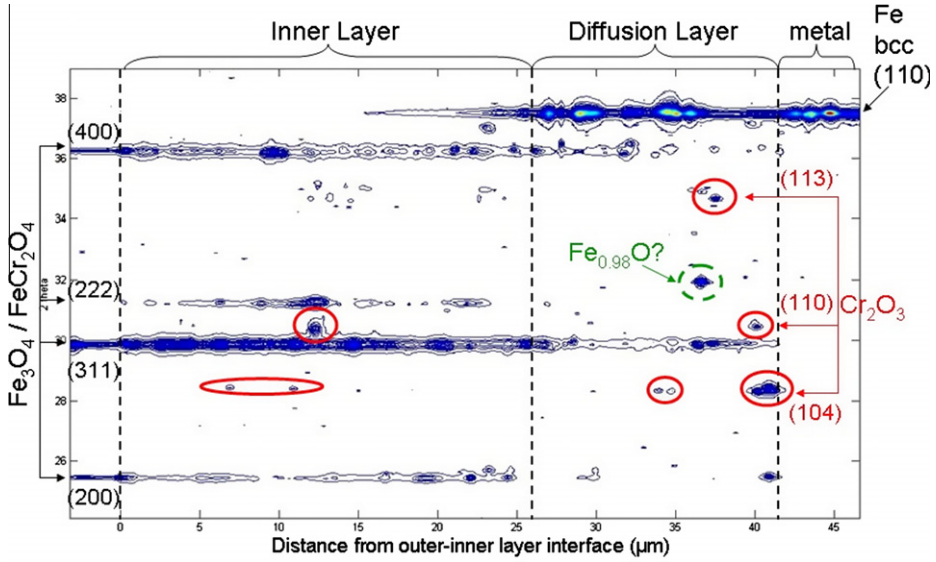

Fig. 8. Contour plot of the synchrotron diffraction intensity as a function of distance in the oxide in the horizontal axis and diffraction angle 2-theta in the vertical axis for the 9CrODS 600 °C 6-week sample.

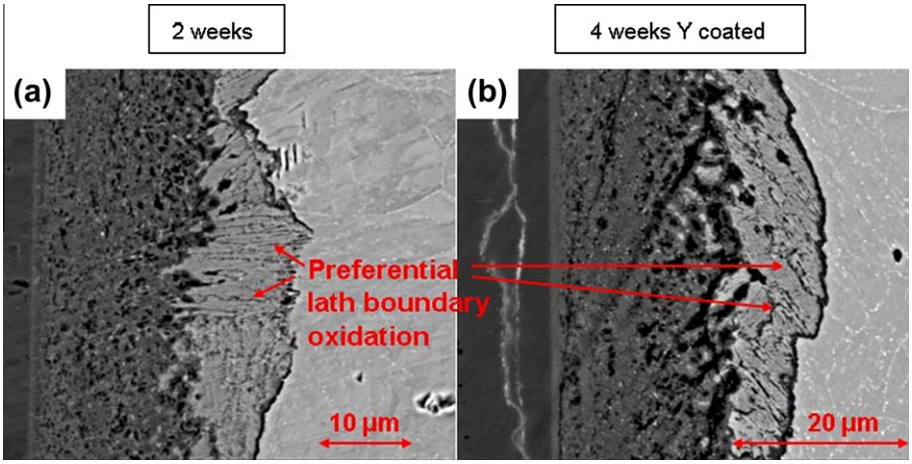

Fig. 9. SEM images of the diffusion layer of HCM12A exposed to 600 °C SCW for (a) 2 weeks and (b) 4 weeks [11].

For example, Fig. 10 shows oxygen, chromium and iron EFTEM maps of the diffusion layer of the 9CrODS 600 °C 2-week sample, which exhibits these large chromium-rich oxide precipitates. The iron and chromium maps complement each other since chromium-rich regions are iron-depleted and vice-versa. The oxygen map shows strong enhancement at the location of chromium enrichment zones. Additionally, a difference in contrast is observed between the oxygen-depleted (iron-rich) regions of the diffusion layer and the metal region: the metal region is much darker, suggesting a lower oxygen content. The shift from the diffusion layer to the metal regions is very sharp and distinct in the oxygen map. The chromium map shows a complementary distribution with stronger intensity in the metal region as compared to the iron-rich regions in the diffusion layer. This suggests that the chromium is evenly distributed in the metal, but once the oxygen reaches an area, elemental segregation occurs, leading to the

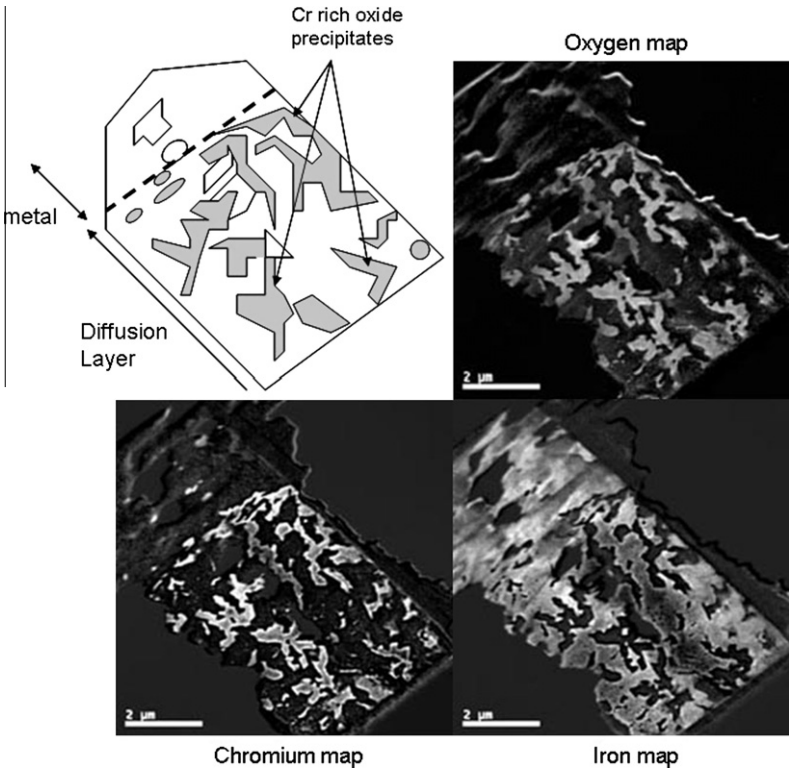

Fig. 10. Oxygen, chromium and iron EFTEM maps of the diffusion layer of the 9CrODS 600 °C 2-week sample, showing large chromium-rich oxide precipitates.

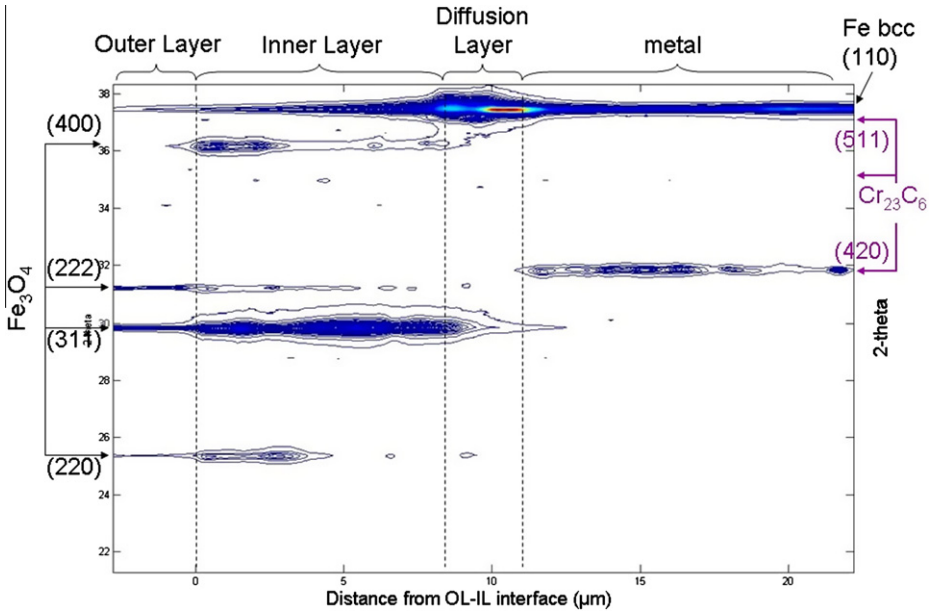

Fig. 11. Contour plot of the microbeam synchrotron diffraction data as a function of the distance in the oxide and diffraction angle 2-theta for NF616 exposed to 500 °C SCW for 8 weeks.

formation of chromium-rich and iron-rich zones. Finally, the iron signal is more intense in the metal than in the diffusion layer, probably due to outward migration of iron in the latter layer.

These large chromium-rich precipitates are located at the lath and metal grain boundaries where chromium carbides are observed in the non-ODS alloys. Consequently, it seems that the chromium necessary to form these chromium-rich oxides may come from the oxidation of the carbides located there as was suggested in a previous article [11]. This is consistent with microbeam synchrotron data showing a disappearance of peaks associated with $Cr_{23}C_6$ in the diffusion layer. Fig. 11 shows a contour plot of the microbeam synchrotron diffraction data as a function of the distance in the oxide for NF616 exposed to 500 °C SCW for 8 weeks. This plot clearly demonstrates the presence of $Cr_{23}C_6$ in the metal but not in the diffusion layer suggesting that the carbides are oxidized in the diffusion layer. In some cases sporadic carbide peaks are observed in the oxide layers but overall most of the carbides present at the grain and lath boundaries are oxidized to form chromium-rich oxide precipitates there.

These large chromium-rich precipitates surround metal grains that appear to be depleted in chromium but still contain some oxygen as was observed in Fig. 10. The presence of oxygen is interesting since oxygen has a negligible solubility in iron and therefore would not be expected in metal grains. Fig. 12 shows EFTEM close-up iron, chromium and oxygen maps of a metal grain of the same 9CrODS 600 °C 2-week sample of Fig. 10. These maps show small, elongated nanometric chromium-rich oxide precipitates (about 100 nm in length and 20 nm in width) within these metal grains that are aligned perpendicular one-to-another. The precipitates form an iron-chromium elemental separation similar to the one observed in the inner layer as was shown a previous article [53]. Such an elemental segregation is not observed within the large chromium-rich precipitates along the lath boundaries. Additionally, neither precipitates nor elemental segregation between chromium and iron were observed on the metal side of the interface. This suggests that the elemental separation only occurs in the presence of oxygen and is linked with the nucleation of the small chromium-rich oxide particles due to the low solubility of oxygen in iron.

3.2. Marker experiment

Fig. 13 shows two SEM images of HCM12A and NF616 samples exposed to 500 °C SCW for 6 weeks, and on which palladium markers had been deposited on the alloy surface prior to oxidation. This experiment was performed to confirm the location of the original water–metal interface as described in more detail in a previous article [12]. After oxidation, the markers are located at the outer–inner layer interface. This confirms the suggested mechanism of oxidation of ferritic–martensitic steels with an outward migration of iron to form the outer layer and an inward migration of oxygen to form the inner layer. Fig. 14 shows a schematic of this oxidation mechanism.

3.3. Comparison of the corrosion resistance of ODS and non-ODS steels

To investigate the corrosion resistance of ODS vs. that of non-ODS steels, the oxidation behavior of the 9CrODS and NF616 alloys

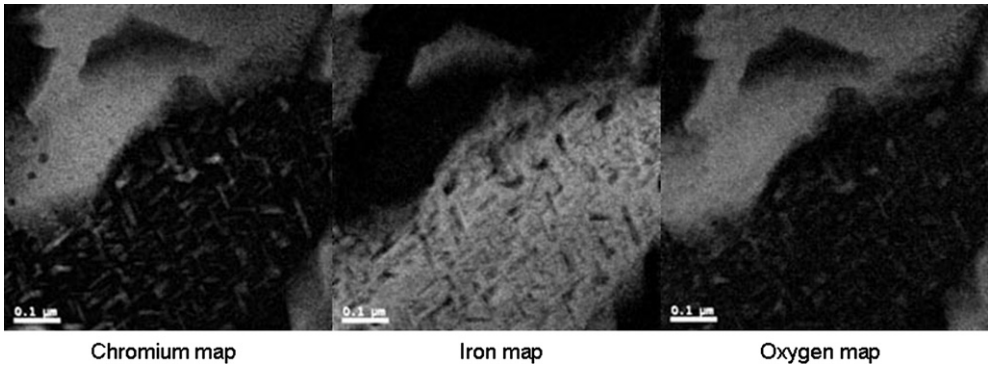

Fig. 12. Iron, chromium and oxygen EFTEM maps of a metal grain of the same 9CrODS 600 °C 2-week.

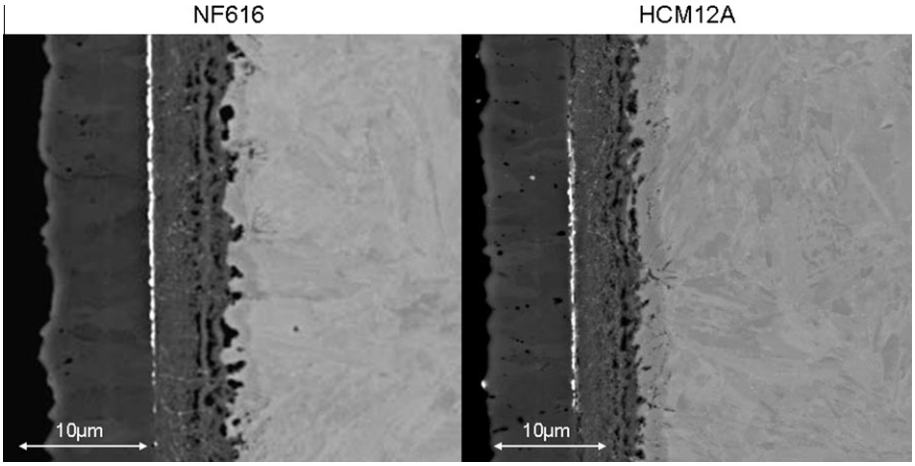

Fig. 13. SEM images of HCM12A and NF616 samples exposed to 500 °C SCW for 6 weeks showing the palladium markers deposited on the alloy surface prior to oxidation.

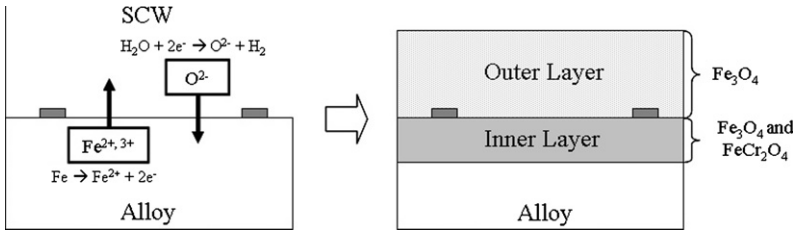

Fig. 14. Schematic of the overall oxidation mechanism.

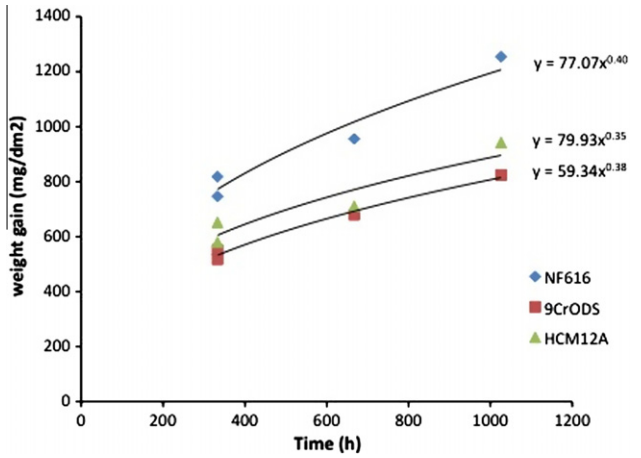

Fig. 15. Weight gain vs. time curve for NF616, HCM12A and the 9CrODS alloys exposed to 600 °C SCW.

was compared since the chromium content of these alloys is similar (9 wt%), and so should corrode at similar rates. Fig. 15 shows the weight gain curve for NF616, HCM12A and the 9CrODS alloy exposed to 600 °C SCW. The 9CrODS steel has the lowest weight gain, even lower than that of a 12 wt% Cr alloy like HCM12A, indicating that the corrosion resistance of ODS alloys is higher than that of conventional ferritic–martensitic alloys [7,8]. These differences in oxidation behavior are associated with differences in oxide microstructure as shown in a previous article [8]. From our results, it is difficult to distinguish at first the effect of the smaller grain size observed in ODS alloys from that the specific effect of the Y–Ti–O nano-particles on the diffusion processes driving the oxidation behavior. Nevertheless, a study of the influence of grain size on the corrosion behavior of T91 by comparing as-received samples with nano-crystallized samples showed only a minor impact of the change in grain size on the corrosion of T91 [56]. Since we observe a significant change in oxidation behavior, the effect in our results is more important, which suggests a certain effect of the Y–Ti–O nano-particles on the oxidation behavior.

Both NF616 and the 9CrODS alloy exhibit a three-layer structure with an outer layer of large columnar grains of Fe_3O_4, an inner layer containing small equiaxed $(Fe,Cr)_3O_4$ spinel grains, and a diffusion layer containing a mixture of oxide precipitates and metal grains. Additionally, in both cases the inner layer is enriched in chromium. Nevertheless, some microstructural differences exist between the oxide layers formed on these two alloys [8].

First the morphology of the oxide layers is different since the diffusion layer in the 9CrODS alloy is much ticker than that in NF616. The 14CrODS alloy also exhibits a large diffusion layer especially compared to the inner layer. For the 9CrODS 600 °C 2-week sample the diffusion-to-inner layer thickness ratio is about 3 while for the NF616 600 °C 2-week sample it is only 0.34. Thus in the ODS alloys studied, the diffusion layer was observed to be thicker than the inner layer.

The second major difference is the chromium enrichments localized at the oxide layer interfaces, especially at the inner-diffusion layer interface and the diffusion layer–metal interface for the 9CrODS alloy but not for NF616 [8,10]. Consequently, it appears the addition of yttrium through the Y–Ti–O particles helps to segregate chromium at specific interfaces (especially the inner-diffusion layer and the diffusion layer–metal interfaces).

The third major difference concerns the increased chromium-rich oxide content (especially Cr_2O_3) in the ODS alloys. Once again, comparing the amount of Cr_2O_3 observed in the diffraction plots of the 9CrODS and NF616 alloys in 600 °C SCW, the NF616 samples show almost no Cr_2O_3, while it was present in significant quantities at the interfaces of the 9CrODS samples [8,10].

From these observations we can investigate how the Y–Ti–O particles influence the oxidation mechanism of ferritic–martensitic steels. It has been proposed that by serving as nucleation sites for the oxide they reduce the amount of chromium needed to form Cr_2O_3, thus making it possible to form Cr_2O_3 in alloys with low chromium content [57,58]. The formation of Cr_2O_3 is important for corrosion resistance since it slows down the diffusion of oxygen and iron [55,59]. Second, yttrium from Y–Ti–O particles has been shown to segregate to oxide grain boundaries, (though to a lesser extent than if the yttrium was in solution), thus helping to inhibit oxide grain growth and slowing down diffusion processes, more specifically the diffusion of iron [6,57,58]. As some yttrium segregates to the grain boundaries it may be also accompanied by oxygen as both elements were combined in the Y–Ti–O particles. The additional oxygen from the Y–Ti–O particles may explain the thicker diffusion layers observed in ODS alloys since such oxygen is used to form the chromium-rich precipitates found at the grain boundaries. In the same way, as was described in Section 2.1, ODS alloys contain much smaller grains, which facilitates the diffusion of elements to grain boundaries. This can also explain the presence of more chromium at these grain boundaries and the formation of more chromium-rich oxides in ODS alloys, especially since the chromium is not trapped in carbides in the ODS alloys. The formation of these chromium-rich oxides leads to slower corrosion, since both iron and oxygen diffusion decreases with chromium content in the oxide [23,55].

3.4. Influence of the corrosion environment (steam vs. SCW)

Fig. 16 shows the weight gain curves for NF616, HCM12A and 14CrODS exposed to SCW and to steam, both at 500 °C. This plot shows that the samples exposed to SCW corroded about 1.5–2 times more than those exposed to steam. This demonstrates an influence of the environment on the corrosion process as described in a previous article [12]. Once again, this variation in oxidation behavior is associated with differences in oxide microstructure. Although a three-layer structure was observed in both cases, overall the oxides formed in steam exhibited denser layers and more Cr_2O_3 was detected, especially at the inner-diffusion layer and diffusion layer-metal interfaces [12,60].

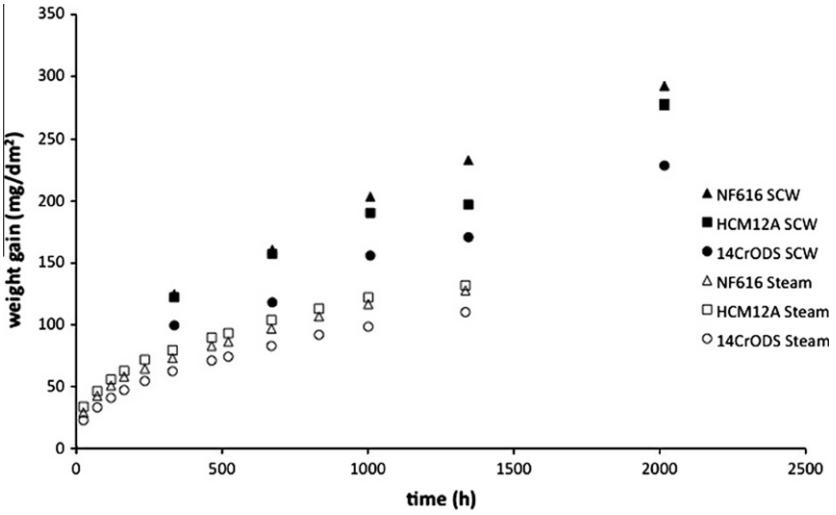

Fig. 16. Weight gain vs. time curves for NF616, HCM12A and 14CrODS exposed to SCW and to steam, both at 500 °C.

Previous work on the oxidation of zirconium alloys in both steam and SCW has shown no influence of the environment of the oxidation behavior [61]. The fact that such a difference is seen in the alloys studied in this project suggests that the rate-limiting step is different in the two cases. In zirconium alloy corrosion a monolayer of ZrO_2 is formed solely by inward migration of oxygen, with the diffusion of corrosion species through the dense layer being the rate-limiting step. The formation of a multi-layer oxide in ferritic–martensitic alloys is more complex: the outward migration of iron forms the outer layer and the inward migration of oxygen forms the inner layer. The different oxidation behavior observed between zirconium and ferritic–martensitic alloys suggests that the outward iron migration is the rate-limiting step, as was found in the literature [2,14–16,62]. Such a conclusion is consistent with the presence of a diffusion layer in the samples since if oxygen diffusion were the rate-limiting step a diffusion layer would be unlikely to form because the oxygen would not diffuse ahead of the oxide.

The main difference between steam and SCW is a difference in pressure leading to a higher density of SCW compared to steam. This higher density will increase the amount of oxidizing agents adsorbed on the oxide surface, and therefore oxidizing at a greater rate the iron present in the outer layer. Consequently, the outer layer surface of samples oxidized in SCW will contain more Fe^{3+} and iron vacancies compared to the outer layer from steam samples. This results in a lower Fe^{2+}/Fe^{3+} ratio at the outer layer surface in SCW compared to steam, which increases the driving force for iron outward migration, thus leading to enhanced corrosion [12]. The additional iron vacancies will form additional pores near the inner-diffusion layer interface as observed in the SCW samples.

Therefore, the analysis of the influence of the corrosion environment on the oxidation behavior of ferritic–martensitic alloys suggests that the rate-limiting step is the outward diffusion of iron and that the main driving force for this outward iron diffusion may be the gradient in the Fe^{2+}/Fe^{3+} ratio through the oxide.

4. Discussion

4.1. Calculation of the outward migration of iron

From the results presented above, it appears like the rate-limiting step for the oxidation of ferritic–martensitic and ODS steels is the outward diffusion of iron from the inner and diffusion layers to form the outer layer. This outward iron diffusion explains the enrichment in chromium observed in the inner and diffusion layers but does the iron leaving these two layers account for all the iron needed to form the outer layer? To answer this question we used the microbeam synchrotron fluorescence data to calculate the difference between the iron concentration in the metal region that will later form the inner layer and in the inner layer after oxidation. For this calculation, we quantitatively estimated the porosity fraction in the inner layer from SEM images, since we suppose that the pores are caused by iron migration. The pore area fraction was measured using the ImageJ program to obtain binary images of the inner layer. This calculation of the porosity fraction brings a relatively large uncertainty in the calculations, which was taken into account.

In the calculation presented below, n_i corresponds to the moles of the species i in the specific layer, c_i corresponds to the concentration of species i in the layer, Δc_{Fe} is the iron concentration difference between the initial iron concentration and the concentration at time t, and x is the chromium concentration in the inner layer when we assume that the average inner layer composition is $Fe_{3-x}Cr_xO_4$. Thus we assume that the inner layer only contains an iron-chromium spinel phase, which enables us to calculate x from concentration ratios obtained from the fluorescence data as shown in the following equation:

$$\frac{c_{Cr_{IL}}}{c_{Fe_{IL}}} = \frac{x}{3-x} \tag{1}$$

Eqs. (2-7) describe the terms used in the calculation.

$$\begin{aligned} c_{Fe_{OL}} &= \frac{n_{Fe_{OL}}}{n_{Fe_{OL}} + n_{O_{OL}}} \qquad c_{O_{OL}} = \frac{n_{O_{OL}}}{n_{Fe_{OL}} + n_{O_{OL}}} \\ c_{Fe_{IL}} &= \frac{n_{Fe_{IL}}}{n_{Fe_{IL}} + n_{Cr_{IL}} + n_{O_{IL}}} \qquad c_{Cr_{IL}} = \frac{n_{Cr_{IL}}}{n_{Fe_{IL}} + n_{Cr_{IL}} + n_{O_{IL}}} \\ c_{Fe_{metal}} &= \frac{n_{Fe_{metal}}}{n_{Fe_{metal}} + n_{Cr_{metal}}} \qquad c_{Cr_{metal}} = \frac{n_{Cr_{metal}}}{n_{Fe_{metal}} + n_{Cr_{metal}}} \end{aligned} \tag{2-7}$$

The difference in iron concentration is then calculated using the formula shown in Eq. (8):

$$\begin{aligned} \Delta c_{Fe_{IL}} &= \frac{n_{Fe_{metal}}}{n_{Fe_{metal}} + n_{Cr_{metal}}} - \frac{n_{Fe_{IL}}}{n_{Fe_{IL}} + n_{Cr_{IL}} + n_{O_{IL}}} = \frac{1}{1 + \frac{c_{Cr_{metal}}}{c_{Fe_{metal}}}} - \frac{1}{1 + \frac{4}{3-x} + \frac{c_{Cr_{IL}}}{c_{Fe_{IL}}}} \\ n_{O_{IL}} &= \frac{4}{3-x} n_{Fe_{IL}} \end{aligned} \tag{8}$$

From the calculation of the difference in iron concentration we can calculate the outer layer thickness that would be formed using

the iron leaving the inner layer. For this we added a term to account for the iron diffusing outwards and leaving pores in the inner layer. The porosity term is simply given by the porosity fraction γ multiplied by the inner layer thickness. Consequently, the calculated outer layer thickness is given by the following formula:

$$h_{OL} = \Delta c_{Fe_{IL}} h_{IL} \times PBR + \gamma h_{IL} \quad (9)$$

where *PBR* corresponds to the Pillings–Bedworth ratio. In this case (Fe_3O_4) the *PBR*, is equal to 2.086.

Figs. 17 and 18 show the results of the calculated outer layer thickness values compared with the thicknesses measured from the SEM images for the samples exposed to SCW at 600 °C and 500 °C, respectively. If just enough iron is released to form the outer layer, the two columns should match. The NF616 and HCM12A alloys show a good fit between the two columns whereas the ODS samples show larger differences between the measured and calculated values. This discrepancy in the ODS samples is likely due to the presence of a large diffusion layer which is difficult to account for fully in the calculations leading to an underestimation of the outer layer thickness. These plots show that in general the iron leaving the inner layer can to a good approximation account for the formation of the entire outer layer.

4.2. Analysis of the bonds in the spinel structure and their impact on diffusion

The bonding of transition metal ions with oxygen ions is in between an ionic and a covalent bond due to the strong interaction between the oxygen 2p orbitals and the metallic 3d orbitals. The covalency of the bond is determined by the energy difference between the O 2p and the metallic 3d orbitals, which in turn reflects the level of hybridization occurring between the oxygen and metal ions. Because hybridization decreases with increasing 3d energy, since Cr 3d energy is lower than that of Fe, one would expect more covalent Cr–O bonds relative to Fe–O bonds [63]. This is confirmed by an electronic transfer of 0.675|e| for chromium compared to only 0.382|e| for iron making the Fe–O bond more ionic [64]. A chromium or iron cation in an octahedral or tetrahedral site can

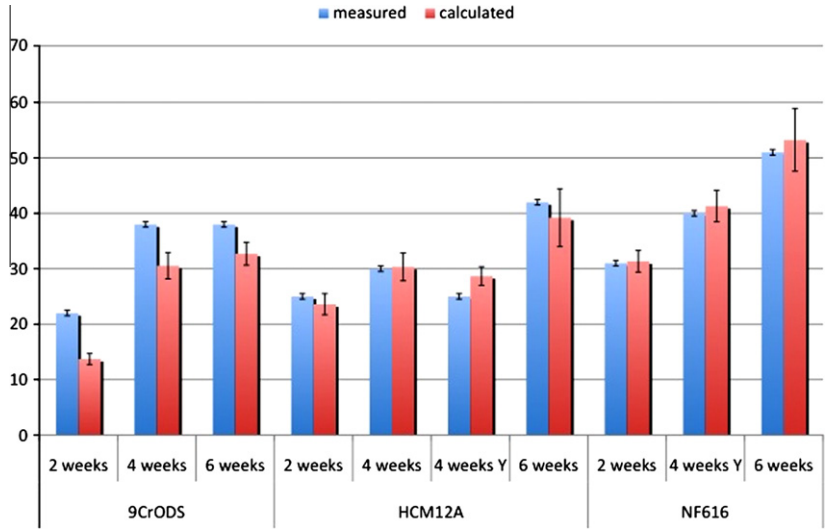

Fig. 17. Bar plot of the calculated outer layer thickness values compared with the thicknesses measured from the SEM images for the samples exposed to SCW at 600 °C. The *Y* corresponds to samples implanted with an yttrium layer on the surface prior to oxidation.

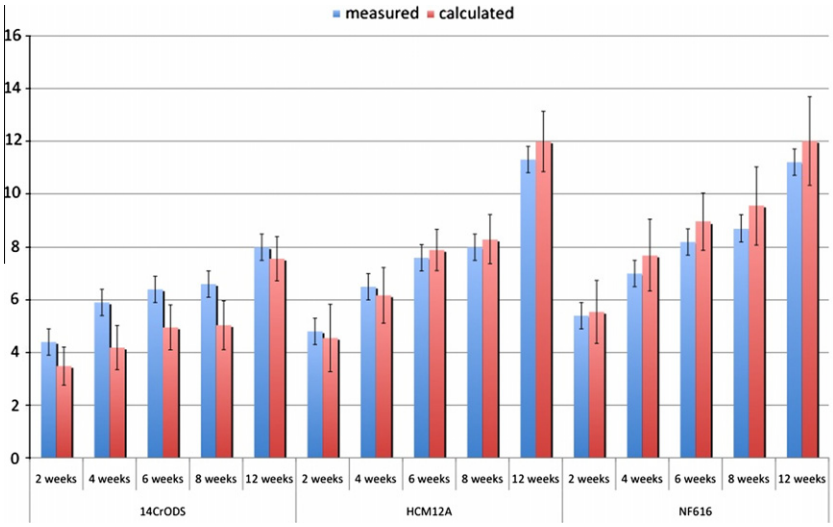

Fig. 18. Bar plot of the calculated outer layer thickness values compared with the thicknesses measured from the SEM images for the samples exposed to SCW at 500 °C.

be considered as a $(FeO_6)^{10-,\,9-}$ or $(FeO_4)^{6-,\,5-}$ ligand complex and therefore it is interesting to study the Fe–O and Cr–O bonds using the ligand field theory [65].

In an octahedral and tetrahedral symmetry, the 3d orbitals are split into two sets of orbitals: three t_{2g} and two e_g orbitals, originating from the interaction of the ligand's orbitals with the d_{xy}, d_{xz}, d_{yz}, and with the d_{x2-y2}, and d_{z2} orbitals, respectively [66]. The splitting amplitude depends on several factors including the cation, ligand strength and especially the degree of hybridization. In an octahedral configuration, the three t_{2g} orbitals are stabilized and have lower energies, and the e_g orbitals are destabilized and have higher energies. This splitting is inversed in tetrahedral sites where the e_g orbitals are lower in energy compared to the t_{2g} orbitals.

The chromium–oxygen interaction is stronger causing a larger splitting, but since Cr^{3+} only has three electrons in the 3d orbitals, there is only one configuration possible with the three unpaired electrons in the t_{2g} orbitals. This leads to a strong stabilization of the Cr^{3+} ion in the octahedral configuration (1.2 Δ_o^{cr}) compared to Fe^{3+}, which has no stabilization (0 Δ_o^{Fe}). The Fe^{2+} ion has a d^6 configuration (six electrons in the 3d orbitals) so four electrons in the t_{2g} (one pairing) and two in the e_g leading to a stabilization of 0.4 Δ_o^{Fe}. This can explain the preferential inverse spinel structure for Fe_3O_4 (stabilization of Fe^{2+} in octahedral sites) compared to the normal spinel structure for $FeCr_2O_4$ (stabilization of Cr^{3+} in octahedral sites and Fe^{2+} in tetrahedral sites (though smaller than its stabilization in octahedral sites)).

Furthermore, the e_g orbitals interact with the oxygen 2p orbitals to form the strong σ-bonds, while the t_{2g} form the weaker ligand-to-metal π-bonds. Since the O^{2-} orbitals are full, they will fill up all the bonding orbitals leaving the metallic 3d electrons to fill the π^* and σ^* anti-bonding orbitals. The σ-bonding creates the more covalent character of the bond, therefore since iron contains two electrons in the e_g states, thus filling σ^* anti-bonding orbitals, the Fe–O bond will have a weaker covalent character compared to the Cr–O bond, where no electrons are found in the σ^* anti-bonding orbitals.

All this suggests that the chromium ion will be too tightly bound to be able to diffuse in the spinel structure. This explains why chromium does not diffuse outwards like iron and remains in the inner layer. Additionally, because chromium is so stable in the octahedral sites compared to iron, its presence in the spinel structure inhibits cation diffusion, thus slowing down the diffusion of iron. This explains the decrease in iron diffusion as the chromium content increases [23]. The diffusion of iron in the spinel structure occurs primarily as Fe^{2+} through octahedral sites as was confirmed by Gillot et al. in their study of the conductivity of spinel when it is oxidized into maghemite (γ-Fe_2O_3) [40,41]. The outward diffusion of Fe^{2+} also serves as an outward diffusion of electrons since the presence of both Fe^{2+} and Fe^{3+} in octahedral sites of Fe_3O_4 allow for quick electron transfer between the two, resulting in an inward diffusion of Fe^{3+} as Fe^{2+} diffuses outwards. This analysis of the diffusion of iron in the spinel structure reinforces a mechanism governed by the diffusion of Fe^{2+} due to a gradient of the Fe^{2+}/Fe^{3+} ratio between the oxide–metal interface and the outer layer surface [12].

4.3. Oxidation mechanism

Fig. 19 shows the early oxidation stage and the diffusion of species once the oxide layers have formed. In the beginning, the oxygen adsorbs on the metal surface creating iron vacancies; this process starts to form the outer layer in association with the outwards diffusion of iron. Since the outer layer grows outward from the metal surface, it is not constrained, which leads to the formation of large columnar grains of Fe_3O_4. In turn, the oxygen penetrates the metal preferentially at the grain and lath boundaries, where it begins to oxidize the chromium carbides, creating chromium-rich oxides on the lath and grain boundaries. The iron from within the grain begins to migrate outwards, drawn by the presence of iron vacancies, thereby enriching the grain it has left in chromium and decreasing the minimum oxygen potential necessary for oxide formation. Simultaneously, the oxygen diffuses inside the grains from the oxide–metal interface and from the surrounding oxygen at the grain boundaries, slowly increasing the oxygen potential within the grain. Because the solubility of oxygen in iron is negligible, nanometric chromium-rich oxides start to from as shown in Fig. 12 [43,53]. The inner layer starts to form once the oxygen potential and the chromium enrichment within the grain reach a critical level. Simultaneously, the oxygen still continues to diffuse beyond the inner layer through grain boundaries, resulting in the formation of the diffusion layer.

Once both layers have formed, the overall oxide layer growth occurs at two interfaces: the outer layer-SCW interface and the inner-diffusion layer interface. The outer layer grows by adsorption of oxygen on the surface creating iron vacancies, which migrate inwards along with electron holes, forcing the iron outwards. This is represented in the Kröger–Vink notations as follows [67]:

$$\begin{aligned} &4H_2O \rightarrow 4O_o + 4H_2 + V''_{Fe} + 2V'''_{Fe} + 8h^*_e \\ &or \\ &2O_2 \rightarrow 4O_o + V''_{Fe} + 2V'''_{Fe} + 8h^*_e \end{aligned} \qquad (10)$$

The Kröger–Vink notation describes point defects and regular atoms in a lattice. The major symbol indicates a defect or an atom and the subscript corresponds to the site it occupies. The charge is denoted by superscripts with a dot (*) being a positive charge and a prime (′) a negative charge. For example, M_M corresponds to a metal atom in a normal metal site and O_O to an oxygen atom in

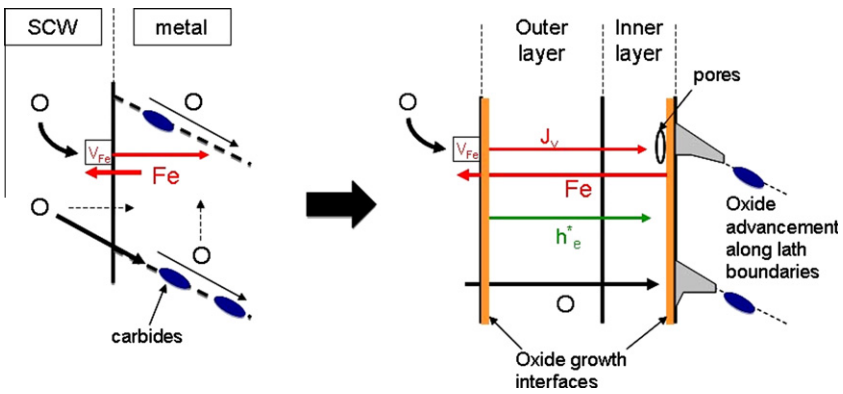

Fig. 19. Schematic of the early oxidation stage and oxidation mechanism with the diffusion of species once the oxide layers have formed.

a normal oxygen site. V_{Fe} is a metal vacancy, V_O an oxygen vacancy, and h_e is an electron hole. The oxidation state of the metal ions is denoted with a roman numeral superscript. This notation does not differentiate between tetrahedral and octahedral sites. In this context since the iron can occupy two different sites in spinel, it is useful to distinguish these by denominating metal vacancies instead by V_{tetra} and V_{octa}. Thus Eq. (10) become:

$$\begin{aligned} &4H_2O \rightarrow 4O_o + 4H_2 + V'''_{tetra} + V'''_{octa} + V''_{octa} + 8h^*_e \\ &or \\ &2O_2 \rightarrow 4O_o + V'''_{tetra} + V'''_{octa} + V''_{octa} + 8h^*_e \end{aligned} \quad (11)$$

The inward migration of vacancies will engender an agglomeration of vacancies at the inner-diffusion layer interface, where we find chromium-rich oxides and a lower oxygen potential. The presence of chromium-rich oxides will hinder the diffusion of iron from the diffusion layer, which is then as a consequence not able to compensate for the influx of vacancies that end up coalescing into pores. In the diffusion layer and at the inner-diffusion layer interface, the iron is oxidized by the combined presence of vacancies and electron holes, as follows:

$$2h^*_e + V''_{octa} + Fe \rightarrow Fe^{II}_{octa} \quad (12)$$

The presence of additional electron holes will oxidize Fe^{2+} into Fe^{3+} according to:

$$h^*_e + Fe^{II}_{octa} \rightarrow Fe^{III}_{octa} \quad (13)$$

Overall, Fe^{2+} ions correspond to electron carriers and Fe^{3+} to electron hole carriers, resulting in fast conduction through the oxide layers, thus suggesting that electron transfer through the oxide is not the rate-limiting step. The iron diffusion through the oxide is assumed to be primarily through a vacancy mechanism, making the oxide a p-type semiconductor, in which electron hole transfer is the main mechanism of electronic conduction. Consequently, the electrons necessary for the reduction of oxygen on the oxide surface come from the Fe^{2+} ions at the surface becoming oxidized into Fe^{3+}. This leads to a gradient of the Fe^{2+} to Fe^{3+} ratio between the outer layer surface and the inner-diffusion layer interface, which creates the necessary conduction of electrons for the red-ox reactions to take place. The outer oxide layer surface contains more Fe^{3+} (and thus a lower Fe^{2+}/Fe^{3+} ratio) than the oxide–metal interface. Since Fe^{2+} and Fe^{3+} ions behave differently in the spinel structure, a simple iron concentration gradient cannot explain the outward iron migration, which is instead driven by a gradient in the Fe^{2+}/Fe^{3+} ratio. This is consistent with results from studies of the corrosion of ferritic–martensitic alloys in SCW containing 2 ppm of dissolved oxygen, showing the presence of Fe_2O_3 at the outer layer surface due to greater availability of oxygen at the oxide surface resulting in the oxidation of all the Fe^{2+} into Fe^{3+} [68,69]. In the same way, the Fe^{2+}/Fe^{3+} ratio is higher near the inner-diffusion layer interface, where FeO was occasionally observed for samples corroded in 600 °C SCW.

Additionally, chromium oxidizes into octahedral sites near the oxide–metal interface according to the following reaction:

$$3h^*_e + V'''_{octa} + Cr \rightarrow Cr^{III}_{octa} \quad (14)$$

As stated in Section 4.2, chromium ions are only located in octahedral sites and force the Fe^{2+} ions into the tetrahedral sites so the oxidation of chromium can be better represented by the following reaction:

$$3h^*_e + V'''_{octa} + Cr + Fe^{II}_{octa} + Fe^{III}_{octa} \rightarrow Cr^{III}_{octa} + Fe^{II}_{tetra} + Fe^{III}_{octa} \quad (15)$$

The presence of chromium decreases the conduction through electron holes by diminishing the number of Fe^{2+} present in octahedral sites, therefore hindering the transfer of electrons between the Fe^{2+} and Fe^{3+} in these sites. This then affects the overall corrosion rate by inhibiting the outward migration of Fe^{2+}.

In summary, the oxidation mechanism for the corrosion of ferritic–martensitic steels is very complex and governed by the outward migration of iron and variations in the oxygen potential. While it is difficult to precisely quantify the oxide layer growth, the iron migrating outwards from the inner and diffusion layers seems to account for most of the iron needed for the outer layer formation. The advancement of the inner layer into the diffusion layer likely occurs when the oxygen potential and the local chromium enrichment reach a level high enough to enable the formation of the iron-rich spinel $(Fe,Cr)_3O_4$. This will create a large outward flux of iron ions that will modify the chromium concentration profile in the inner layer and leave a new chromium enriched region at the new inner-diffusion layer interface.

5. Conclusion

Ferritic and martensitic steels are primary candidates for application in several Generation IV reactors, especially the Supercritical Water Reactor. Since corrosion is one of the main issues for these alloys in the harsh environments of the reactor core, understanding the oxidation behavior of these alloys may help find solutions to minimize corrosion, and increase the potential utilization of these alloys. In this article we analyzed the microstructure of the oxide formed on these alloys, and to study the relationship between the microstructure and the oxidation behavior, so as to derive insight on the oxidation mechanism. The oxide layers were characterized using microbeam synchrotron radiation diffraction and fluorescence, and electron microscopy (both scanning and electron microscopy).

The main experimental results from this project are the following:

1. The oxide formed a three-layer structure. The outer layer contained large columnar grains of Fe_3O_4, the inner layer contained a mixture of Fe_3O_4 and $FeCr_2O_4$ in small equiaxed grains, and the diffusion layer contained a mixture of metal grains and chromium rich oxide precipitates ($FeCr_2O_4$ and Cr_2O_3). Finally porosity was observed in the inner layer, primarily located at the inner-diffusion layer interface.
2. Small, localized phases such as Cr_2O_3 detected at the interfaces appeared to have an impact on the corrosion resistance. For example, the ODS alloys and steam samples contained more Cr_2O_3 at the inner-diffusion layer interface or the diffusion layer-metal interface and also exhibited lower corrosion rates. The presence and location of the Cr_2O_3 phase varied with exposure time for the 9CrODS alloy exposed to SCW at 600 °C.
3. The ODS alloys corroded significantly less than other ferritic–martensitic steels of equivalent chromium content. It is likely due to the presence of the Y–Ti–O particles, although the exact mechanism is still unknown.
4. The inner oxide layer was characterized by chromium-rich zones associated with the porosity and a nanometric Fe–Cr separation, which may correspond to the presence of both $FeCr_2O_4$ and Fe_3O_4. This separation is likely due to the fact that $FeCr_2O_4$ has a normal spinel structure while Fe_3O_4 has an inverse spinel structure.
5. In the diffusion layer, micrometric chromium-rich oxide precipitates were observed on the lath and prior austenite grain boundaries. The carbides located on these grain boundaries were for the most part oxidized and the chromium from the carbides served to form the chromium rich oxides.
6. In the diffusion layer, nanometric chromium-rich oxide precipitates (indexed as $FeCr_2O_4$ or a chromium-rich $(Fe,Cr)_3O_4$ phase

of indefinite Fe/Cr ratio) were observed within the metal grains leading to Fe–Cr segregation, which occurred only in the presence of oxygen.
7. The oxide layers formed on the various alloys exhibited very little microstructural variation with exposure time but often showed variations in the chromium content, as measured by the fluorescence data, were seen in the inner layer, which may influence the diffusion coefficients of the various corrosion species.
8. A marker experiment was performed to determine the location of the original water–metal interface after corrosion. A photolithographic technique was used to deposit micrometric markers, which were observed at the outer–inner layer interface after corrosion. This is consistent with an overall oxidation mechanism of iron migrating outwards to form the outer layer and oxygen migrating inwards to form the inner and diffusion layers.
9. Corrosion in steam was found to be slower than in SCW: the weight gain and oxide layer thicknesses were about 1.5–2 times smaller in steam. This difference is associated with the outward diffusion of iron and is likely caused by differences in water density on the sample surface in the two environments.

The analysis of these results leads to the following conclusions concerning the oxidation mechanism:

1. The analysis of the spinel structure suggests that the octahedral sites are the primary diffusion paths and that the Fe^{2+} ion is the main species to diffuse. Electron exchange between the Fe^{2+} and Fe^{3+} ions in the octahedral sites facilitates the electron/electron hole transfer throughout the layers. Finally, the chromium does not migrate since it is well stabilized in the octahedral site. Since chromium is located in the octahedral sites, it reduces the electron exchange (because it does not switch from 2+ to 3+ like iron) and diminishes the available diffusion paths for Fe^{2+}, which explains the slower diffusion and corrosion in higher chromium oxides.
2. Calculations of the amount of iron leaving the inner and diffusion layers accounts for the amount of iron necessary for the formation of the outer layer. This suggests that the dissolution of the oxide layer into SCW is negligible, if any.
3. The analysis of the differences in corrosion behavior observed between the oxidation in steam and in SCW suggests that the rate-limiting step in the oxide formation is the outward migration of iron. The iron migrates up the oxygen potential towards the high oxygen potential located at the outer layer surface, where the Fe^{2+}/Fe^{3+} ratio is smaller than at the inner-diffusion layer interface. Fe^{2+} ions are electron carriers and Fe^{3+} ions are electron hole carriers helping in the transfer of electrons necessary for the redox reactions to occur.
4. As the Fe^{2+} ions are oxidized into Fe^{3+} in the outer layer, vacancies are created to preserve the electro-neutrality of the oxide. These vacancies then migrate inwards as the iron migrates outwards until they reach the inner-diffusion layer interface, where they accumulate and coalesce into pores. The pores then form at the location with the lowest oxygen potential.

From these conclusions we propose the following step-by-step advancement of the inner layer into the diffusion layer:

1. Oxygen diffuses ahead of the oxide along the lath and grain boundaries, oxidizing the carbides present at these boundaries and forming chromium-rich oxides. This process forms the diffusion layer.
2. At the same time the oxidized iron in the inner layer and the diffusion layer migrates outwards to form the outer layer, leaving pores and a localized chromium enrichment at the inner-diffusion layer interface.
3. The oxygen diffuses within the metal grains of the diffusion layer immediately forming nanometric chromium-rich spinel oxide precipitates because of the negligible oxygen solubility in iron.
4. When the oxygen potential is high enough to form Fe_3O_4 within these metal grains of the diffusion layer, the iron is oxidized and the inner layer advances into the diffusion layer.
5. This creates a large outward flux of iron ions towards the outer layer, which causes the chromium enrichment located at the previous inner-diffusion layer interface to disappear. The pores that were present there are replenished. As the iron migrates outwards, a new enrichment appears at the new inner-diffusion layer interface.

To conclude, we were able to characterize the oxide layer microstructure in several ferritic–martensitic and ODS alloys and obtain some insight on the corrosion mechanism of these alloys. Nevertheless, the mechanism is still not fully understood and further investigation is needed. ODS alloys are more corrosion resistant than conventional ferritic–martensitic steels and therefore might be better suited for application in the Supercritical Water Reactor, but in order to conclude on the application of either the ODS or conventional ferritic–martensitic steels for reactor use with long exposure times, corrosion tests for longer exposure times would be needed.

Acknowledgments

The authors would like to thank Zhonghou Cai for his help acquiring data at the APS in Argonne National Laboratory, and Trevor Clark and Joe Kulik for their help in the TEM sample preparation and examination. The authors would also like to thank Yann de Carlan at the CEA for the use of the 14CrODS alloy produced at the CEA. This publication was supported by the Pennsylvania State University Materials Research Institute Nanofabrication Lab and the National Science Foundation Cooperative Agreement No. 0335765, National Nanotechnology Infrastructure Network, with Cornell University. This study was funded by DOE-NERI Project DE-FC07-06ID14744. The use of the APS was supported by the DOE, Basic Energy Sciences, Office of Science under Contract No. W-31-109-Eng-38.

References

[1] "A Technology Roadmap for Generation IV Nuclear Energy Systems", Report No. GIF002-00, December 1, 2002, http://nuclear.gov.
[2] L. Tan, M.T. Machut, K. Sridharan, T.R. Allen, J. Nucl. Mater. 371 (2007) 161–170.
[3] S. Ohtuska, S. Ukai, M. Fujiwara, T. Kaito, T. Narita, Mater. Trans. 46 (2005) 1.
[4] S. Ukai, S. Mizuta, T. Yoshitake, T. Okuda, M. Fujiwara, S. Hagi, T. Kobayashi, J. Nucl. Mater. 283–287 (2000) 702.
[5] P. Dubuisson, Y. de Carlan, V. Garat, M. Blat, J. Nucl. Mater. (2011), http://dx.doi.org/10.1016/j.jnucmat.2011.10.037.
[6] Y. Chen, K. Sridharan, T.R. Allen, S. Ukai, J. Nucl. Mater. 359 (2006) 50.
[7] Y. Chen, K. Sridharan, S. Ukai, T.R. Allen, J. Nucl. Mater. 371 (2007) 118–128.
[8] J. Bischoff, A.T. Motta, X. Ren, T.R. Allen, in: Proceedings of the 14th Environmental Degradation of Materials In Nuclear Power Systems 2009, American Nuclear Society, 2009, pp. 1764–1770.
[9] J. Bischoff, A.T. Motta, Y. Chen, T.R. Allen, in: Corrosion 2009, March 22, 2009–March 26, 2009. 2009, Atlanta, GA, United states: National Assoc. of Corrosion Engineers International.
[10] J. Bischoff, A.T. Motta, R.J. Comstock, J. Nucl. Mater. 392 (2009) 272–279.
[11] J. Bischoff, A.T. Motta, L. Tan, T.R. Allen. in: Materials for Future Fusion and Fission Technologies, 2–4 December 2008. 2009, Warrendale, PA, USA: Materials Research Society, vol. 1125, pp. 19–24.
[12] J. Bischoff, A.T. Motta, C. Eichfeld, R.J. Comstock, G. Cao, T.R. Allen, J. Nucl. Mater., in press. (NFSM-3 special issue).
[13] L. Martinelli, Mecanisme de corrosion de l'acier T91 par l'eutectique Pb–Bi utilise comme materiau cible de spallation. Thesis for PhD Universite Paris VI, 2005.
[14] L. Martinelli, F. Balbaud-Célérier, G. Picard, G. Santarini, Corros. Sci. 50 (2008) 2549–2559.

[15] L. Martinelli, F. Balbaud-Célérier, A. Terlain, S. Bosonnet, G. Picard, G. Santarini, Corros. Sci. 50 (2008) 2537–2548.
[16] L. Martinelli, F. Balbaud-Célérier, A. Terlain, S. Delpech, G. Santarini, J. Favergeon, G. Moulin, M. Tabarant, G. Picard, Corros. Sci. 50 (2008) 2523–2536.
[17] L. Martinelli, T. Dufrenoy, K. Jaakou, A. Rusanov, F. Balbaud-Célérier, J. Nucl. Mater. 376 (2008) 282–288.
[18] F. Maak, C. Wagner, Werkst. Korros. 12 (1961) 273–277.
[19] C. Wagner, Corros. Sci. 9 (1969) 91–109.
[20] P. Kofstad, High temperature oxidation of metals. The corrosion monograph series, in: N.H.R.T. Foley, C.V. King, F.L. LaQue, H.H. Uhlig, John Wiley & Sons, New York, 1966.
[21] R. Dieckmann, Phys. Chem. Chem. Phys. 86 (1982) 112–118.
[22] R. Dieckmann, H. Schmalzried, Phys. Chem. Chem. Phys. 81 (1977) 414–419.
[23] J. Topfer, S. Aggarwal, R. Dieckmann, Solid State Ionics 81 (1995) 251–266.
[24] A. Brückman, Corros. Sci. 7 (1967) 51–59.
[25] D.P. Whittle, G.C. Wood, Electrochem. Soc. – J. 114 (1967) 986–993.
[26] A. Atkinson, Solid State Ionics 28–30 (1988) 1377–1387.
[27] A. Atkinson, D.W. Smart, J. Electrochem. Soc. 135 (1988) 2886–2893.
[28] A. Brückman, R. Emmerich, S. Mrowec, Oxid. Met. 5 (1972) 137–147.
[29] A. Brückman, J. Romanski, Corros. Sci. 5 (1965) 185–191.
[30] G.B. Gibbs, R. Hales, Corros. Sci. 17 (487–497) (1977) 499–507.
[31] R. Hales, A.C. Hill, Corros. Sci. 12 (1972) 843–853.
[32] J. Robertson, Corros. Sci. 29 (1989) 1275–1291.
[33] J. Robertson, Corros. Sci. 32 (1991) 443–465.
[34] J. Robertson, M.I. Manning, in: Structural and Mechanical Aspects of High Temperature Oxidation, 23 March 1988, 1988, UK, vol. 4: pp. 1064–1071.
[35] J. Robertson, M.I. Manning, in Structural and Mechanical Aspects of High Temperature Oxidation, 20 October 1988, 1989, UK, vol. 5, pp. 741–753.
[36] C. Wang, D.R. Baer, J.E. Amonette, M.H. Engelhard, J. Antony, Y. Qiang, J. Am. Chem. Soc. 131 (2009) 8824–8832.
[37] H.J. Levinstein, M. Robbins, C. Capio, Mater. Res. Bull. 7 (1972) 27–34.
[38] F. Magalhaes, M.C. Pereira, S.E.C. Botrel, J.D. Fabris, W.A. Macedo, R. Mendonça, R.M. Lago, L.C.A. Oliveira, Appl. Catal. A 332 (2007) 115–123.
[39] B. Gillot, D. Delafosse, P. Barret, Mater. Res. Bull. 8 (1973) 1431–1442.
[40] B. Gillot, J.-F. Ferriot, G. Dupré, A. Rousset, Mater. Res. Bull. 11 (1976) 843–849.
[41] B. Gillot, F. Jemmali, F. Chassagneux, C. Salvaing, A. Rousset, J. Solid State Chem. 45 (1982) 317–323.
[42] I. Nedkov, T. Merodiiska, L. Slavov, R.E. Vandenberghe, Y. Kusano, J. Takada, J. Magn. Magn. Mater. 300 (2006) 358–367.
[43] D.E.J. Talbot, J.D.R. Talbot, Corrosion Science and Technology, CRC Press, Taylor & Francis Group, LLC, 2007.
[44] H. Föhl, Ionic Crystals. <http://www.tf.uni-kiel.de/matwis/amat/def_en/kap_2/basics/b2_1_6.html> (03.05.11).
[45] R.L. Klueh, D.R. Harries, High Chromium Ferritic and Martensitic Steels for Nuclear Applications, ASTM, West Conshohocken, PA, 2001.
[46] Y. de Carlan, J.L. Bechade, P. Dubuisson, J.L. Seran, P. Billot, A. Bougault, T. Cozzika, S. Doriot, D. Hamon, J. Henry, M. Ratti, N. Lochet, D. Nunes, P. Olier, T. Leblond, M.H. Mathon, J. Nucl. Mater. 386–388 (2009) 430–432.
[47] K. Sridharan, S.P. Harrington, A.K. Johnson, J.R. Licht, M.H. Anderson, T.R. Allen, Mater. Des. 28 (2007) 1177–1185.
[48] K. Sridharan, A. Zillmer, J.R. Licht, T.R. Allen, M.H. Anderson, L. Tan, in Proceedings of ICAPP 04, Pittsburgh, PA, 2004, p. 537.
[49] A.T. Motta, A.D. Siwy, J.M. Kunkle, J.B. Bischoff, R.J. Comstock, Y. Chen, T.R. Allen, in 13th International Conference on Environmental Degradation of Materials in Nuclear Power Systems 2007, April 19, 2007–April 23, 2007, Whistler, BC, Canada: Canadian Nuclear Society, vol. 3, 2007, pp. 1501–1513.
[50] A. Yilmazbayhan, A.T. Motta, R.J. Comstock, G.P. Sabol, B. Lai, Z. Cai, J. Nucl. Mater. 324 (2004) 6–22.
[51] A. Yilmazbayhan, O. Delaire, A.T. Motta, R.C. Birtcher, J.M. Maser, B. Lai, J. Nucl. Mater. 21 (2003) 221–232.
[52] L.A. Giannuzzi, F.A. Stevie, Micron 30 (1999) 197–204.
[53] J. Bischoff, A.T. Motta, J. Nucl. Mater. (2012) (accepted for publication).
[54] A.D. Siwy, T.E. Clark, A.T. Motta, J. Nucl. Mater. 392 (2009) 280–285.
[55] A.C.S. Sabioni, A.M. Huntz, F. Silva, F. Jomard, Mater. Sci. Eng. A 392 (2005) 254–261.
[56] T.R. Allen, Report "Candidate Materials Evaluation for Supercritical Water-Cooled Reactor", DE-FC07-05ID14664, 2008.
[57] J. Stringer, Oxid. Met. 5 (1972) 11–47.
[58] J. Stringer, Mater. Sci. Eng. A 120 (1989) 129.
[59] Y. Ishikawa, T. Yoshimura, M. Arai, Vacuum 47 (1996) 701–704.
[60] J. Bischoff, A.T. Motta, in: 15th Environmental Degradation of Materials In Nuclear Power Systems 2011, Colorado, Springs, 2011.
[61] A.T. Motta, A. Yilmazbayhan, M. Gomes da Silva, R.J. Comstock, G. Was, J. Busby, E. Gartner, Q. Peng, Y.H. Jeong, J.Y. Park, J. Nucl. Mater. 371 (2007) 61–75.
[62] L. Tan, X. Ren, T.R. Allen, Corros. Sci. 52 (2010) 1520–1528.
[63] F.M.F. de Groot, M. Grioni, J.C. Fuggle, J. Ghijsen, G.A. Sawatzky, H. Petersen, Phys. Rev. B 40 (1989) 5715.
[64] M. Catti, G. Sandrone, G. Valerio, R. Dovesi, J. Phys. Chem. Solids 57 (1996) 1735–1741.
[65] H.L. Schläfer, G. Gliemann, Basic Principles of Ligand Field Theory, Wiley Interscience, New York, 1969.
[66] G.L. Miessler, D.A. Tarr, Inorganic Chemistry, third ed., Pearson/Prentice Hall, 2003.
[67] F.A. Kröger, H.J. Vink, Relations between the concentrations of imperfections in crystalline solids, in: S. Frederick, T. David (Eds.), Solid State Physics, Academic Press, 1956. pp. 307–435.
[68] X. Ren, K. Sridharan, T.R. Allen, J. Nucl. Mater. 358 (2006) 227–234.
[69] L. Tan, Y. Yang, T.R. Allen, Corros. Sci. 48 (2006) 3123–3138.